THE JOURNAL OF BIOLOGICAL CHEMISTRY VOL. 286, NO. 43, pp. 37768–37777, October 28, 2011

Oligomerization and Pore Formation by Equinatoxin II Inhibit Endocytosis and Lead to Plasma Membrane Reorganization*[S]

Received for publication, July 11, 2011, and in revised form, August 29, 2011 Published, JBC Papers in Press, September 1, 2011, DOI 10.1074/jbc.M111.281592

Ana J. García-Sáez[‡§1], Sabine B. Buschhorn[¶], Heiko Keller[‡], Gregor Anderluh[‖2], Kai Simons[¶], and Petra Schwille[‡3]

From the [‡]BIOTEC der TU Dresden, 01307 Dresden, Germany, the [§]Max-Planck Institute for Intelligent Systems and German Cancer Research Center, Bioquant, 69120 Heidelberg, Germany, the [¶]Max-Planck Institute for Cell Biology and Genetics, 01307 Dresden, Germany, and the [‖]Department of Biology, Biotechnical Faculty, University of Ljubljana, 1000 Ljubljana, Slovenia

Pore-forming toxins have evolved to induce membrane injury by formation of pores in the target cell that alter ion homeostasis and lead to cell death. Many pore-forming toxins use cholesterol, sphingolipids, or other raft components as receptors. However, the role of plasma membrane organization for toxin action is not well understood. In this study, we have investigated cellular dynamics during the attack of equinatoxin II, a pore-forming toxin from the sea anemone *Actinia equina*, by combining time lapse three-dimensional live cell imaging, fluorescence recovery after photobleaching, FRET, and fluorescence cross-correlation spectroscopy. Our results show that membrane binding by equinatoxin II is accompanied by extensive plasma membrane reorganization into microscopic domains that resemble coalesced lipid rafts. Pore formation by the toxin induces Ca^{2+} entry into the cytosol, which is accompanied by hydrolysis of phosphatidylinositol 4,5-bisphosphate, plasma membrane blebbing, actin cytoskeleton reorganization, and inhibition of endocytosis. We propose that plasma membrane reorganization into stabilized raft domains is part of the killing strategy of equinatoxin II.

Pore-forming proteins (PFPs)[4] have been developed by many organisms ranging from bacteria and parasites to animals to disrupt membrane integrity of the target cell. The purpose of membrane permeabilization in many cases is to compromise cell survival, as it happens with toxins like α-toxin, actinoporins, or the proteins of the Bcl-2 family and perforin in human cells. However, it can also be related with the escape of certain bacteria from the phagosome, like listeriolysin, or with protein delivery into the cytosol, as in the case of colicins (1–3).

PFPs are secreted by the producer cell in soluble form and bind to target cells via specific receptors. Then they undergo a conformational change that exposes hydrophobic residues and allows their insertion into the plasma membrane and oligomerization into a pore. The nature, stoichiometry, and size of that pore depend on the PFP (1). *In vitro* studies suggest that the toxins of the actinoporin family form a tetramer (4–6), although it could also have a structure similar to those recently reported for cytolysin A or fragaceatoxin C (7, 8), with a higher oligomeric state. The nature of the pore is believed to be toroidal, with lipids exposed to the pore lumen (9). In red blood cells and on artificial lipid vesicles, actinoporins formed pores ~2 nm in diameter (10, 11).

Many PFPs use molecules associated with lipid rafts as receptors (12). Rafts are lipid/protein domains enriched in cholesterol and sphingolipids that act as signaling platforms in the plasma membrane of the cell. During the last years, there has been extensive debate over what rafts are and their functional role. Different domains of raft nature have been observed in several temporal and spatial scales. As a consequence, there are many different kinds of domains that have been associated with rafts (13).

Some examples of raft-associated toxins are aerolysin, which binds to glycosylphosphatidylinositol (GPI)-anchored proteins, cholesterol-dependent cytolysins, or the actinoporins, which bind specifically to sphingomyelin (14–16). Moreover, several PFPs, like parasporin-2, and sticholysin, have been found associated with detergent-resistant membranes, a method that, although not exempt of artifacts, has been used to detect lipid rafts (17, 18).

One interesting example is equinatoxin II (EqtII), a PFP of the sea anemone *Actinia equina* that exhibits lytic activity in several cell types. EqtII belongs to the family of actinoporins and, like the other members of the family, forms pores in sphingomyelin-containing membranes by oligomerization and insertion of an N-terminal α-helix that contributes to the structure of the pore (1, 16). Using model membranes in *in vitro* experiments, we and others have shown that the presence of liquid ordered, raft-like lipid domains promotes EqtII binding and pore activity, with an enrichment of the toxin at the domain interface (19, 20). Recently, a GFP version of EqtII expressed in cells was used to detect sphingomyelin facing the cytosolic side of cellular membranes (21).

Despite their association with lipid raft components, the purpose of lipid raft targeting by PFPs remains unclear. It has been proposed that lipid rafts promote the pore activity by acting as

* This work was supported by funds from the German Cancer Research Center (to A. J. G.-S.) and the Max Planck Society.
[S] The on-line version of this article (available at http://www.jbc.org) contains supplemental Figs. S1–S4 and Movies S1–S7.
[1] To whom correspondence may be addressed: Im Neuenheimer Feld 267, 69120 Heidelberg, Germany. Tel.: 49-6221-54-51234; Fax: 49-6221-54-51482; E-mail: ana.garcia@mf.mpg.de.
[2] Present address: National Institute of Chemistry, Hajdrihova 19, 1000 Ljubljana, Slovenia.
[3] To whom correspondence may be addressed: Tatzberg 47-51, 01307 Dresden, Germany. Tel.: 49-351-463-40328; Fax: 49-351-463-40342; E-mail: petra.schwille@biotec.tu-dresden.de.
[4] The abbreviations used are: PFP, pore-forming protein; GPI, glycosylphosphatidylinositol; EqtII, equinatoxin II; PI(4,5)P_2, phosphatidylinositol 4,5-bisphosphate; LAT, linker of T cell activator; VSV, vesicular stomatitis virus; PCX, podocalyxin; FRAP, fluorescence recovery after photobleaching; ROI, region of interest.

concentration platforms (2). Alternatively, it could be that they participate in determining the target cell specificity or in lowering the energy barrier for pore formation.

In this work, we investigated the cellular alterations induced by EqtII with a focus on the plasma membrane and its organization. We found that EqtII induces a drastic reorganization of the plasma membrane shortly after toxin binding. We observed the formation of immobile, microscopic domains that seem stabilized rafts and correlate with an inhibition of endocytosis and abnormal cytoskeleton structure. At longer times after toxin addition, EqtII induced the growth of a stable bleb in the target cell, concomitant with elevations in cytosolic Ca^{2+} levels that caused degradation of $PI(4,5)P_2$ at the plasma membrane. Altogether, our results show a strong effect of EqtII on the plasma membrane organization of the target cell and suggest a possible role for microscopic domain clustering on its toxic action.

EXPERIMENTAL PROCEDURES

Protein Purification and Labeling—Cysteine mutants of equinatoxin II were purified as described by Malovrh *et al.* (22) and Kristan *et al.* (23). The purified, active EqtII-L26C mutant was labeled with Alexa Fluor 488 C5 maleimide (Invitrogen), Alexa Fluor 555 C5 maleimide (Invitrogen), or Atto655 maleimide (Atto Tech) according to the manufacturer's instructions. The separation of the labeled protein from the free dye was achieved with a 10DG gel filtration column from Bio-Rad. Labeling efficiency was checked by spectroscopy measurements done with a Specord S 100 from Analytik Jena (Jena, Germany). As a negative control for pore activity, we used an EqtII mutant with three cysteines at positions 8, 18, and 69, EqtII mutant (23). A disulfide bond between residues 8 and 69 forms during toxin production, so that the protein loses its hemolytic activity. The third cysteine at position 18 was used for fluorescent labeling with Atto655 maleimide as described above. Prior to the experiments, the unlabeled or labeled triple cysteine mutant was treated either with 0.5 mM 1,10-phenantroline and 0.1 mM $CuSO_4$ for 30 min at 37 °C to ensure the oxidized form of the mutant, EqtII mutant^{oxid}. These concentrations were sufficient to obtain fully oxidized samples.

DNA Constructs and Cell Culture—Myristoylated and palmitoylated yellow fluorescent protein (Myr-Pal-YFP), linker of T cell activator (LAT)-WT-GFP, GPI-GFP, vesicular stomatitis virus glycoprotein 3 (VSV)-sp-GFP and podocalyxin (PCX)-GFP expression constructs have been described in Refs. 24–26. The plasmids encoding for the marker constructs PH(PLCδ1)-EGFP and lifeact-EGFP were kindly provided by Tobias Meyer and Roland Wedlich-Soldner, respectively (27, 28).

HEK293T cells, HeLa Kyoto cells, and COS7 cells were cultured at 37 °C in DMEM (high glucose; Sigma) with 10% fetal calf serum in 5% CO_2. All cells were regularly passaged at subconfluency and plated at 1–5 × 10^4 cells/ml density. For imaging experiments, the cells were seeded in LabTek chambers (Nunc). When required, they were transfected one or 2 days after seeding with 0.2–0.4 ng of the corresponding plasmid DNA using Attractene (Qiagen) according to the manufacturer's protocol. Experiments were carried out 24 or 48 h after seeding or transfection.

Bright Field and Confocal Microscopy—For microscopy experiments, the cells were washed twice with buffer A containing 150 mM NaCl, 20 mM Hepes, pH 7.4, 20 mM trehalose, 15 mM glucose, 5.4 mM KCl, 0.9 mM $MgSO_4$, and 0.5 mM $CaCl_2$ (29). Buffer A with 1 mM EDTA instead of $CaCl_2$ was used for control samples.

For bright field imaging, time lapse imaging with z-stack acquisition after EqtII addition was carried out with a Zeiss Axiovert 200 M inverted microscope at 37 °C. A z-Piezo and a 63× NA1.4 oil objective were used. Transmitted light and fluorescence images (with filters EX 480/30; BS 505; EM 535/40) were acquired sequentially, and the best focus position was selected after the experiments with Metamorph software.

Experiments of membrane reorganization, Ca^{2+}, $PI(4,5)P_2$ degradation, endocytosis, and actin imaging were performed on a Zeiss LSM 510 with a 40× NA1.2 UV-visible IR C Apochromat water objective at room temperature after treatment with 5 μg/ml (250 nM) EqtII-Atto655. Membrane reorganization upon toxin treatment was followed by three-dimensional time lapse imaging of cells transfected the previous day with different membrane markers. For Ca^{2+} imaging, the cells were incubated in 10 μM Fluo-4 acetoxymethyl ester for 20 min at 37 °C and then washed again with buffer A to remove nonincorporated dye. Pictures were taken before and every 20 s after toxin addition. For analysis of $PI(4,5)P_2$ degradation, the cells were transfected with PH(PLC δ1)-EGFP. One day later, time lapse confocal imaging was used to monitor changes in PH(PLC δ1)-EGFP localization after toxin addition. For endocytosis experiments, cholera toxin B subunit labeled with Alexa 488 (CBT-Al488) was added at a concentration of 500 ng/ml and coincubated with EqtII as indicated. After 1 h, confocal images of the samples were acquired, and the degree of endocytosed CTB was quantified by averaging the fluorescence intensity because of CBT-Al488 inside the cells under the same imaging conditions. To monitor changes in actin cytoskeleton, time lapse z-stacks of cells transfected with lifeact-EGFP were acquired after EqtII treatment. Image processing and analysis was performed with Fiji and Volocity software and movies were prepared with Volocity software.

FRAP Measurements—FRAP experiments were performed 1 day after transfection of cells cultured on Labtek chambers with GPI-GFP. Before measuring, the medium in the observation chambers was washed and exchanged with buffer A, and the cells were treated or not with 5 μg/ml EqtII for 1 h at room temperature.

FRAP was performed using a confocal laser scanning microscope LSM510 (Zeiss) with a 40× NA 1.2 UV-visible IR C Apochromat water objective and a fully open pinhole. The measurements were carried out at room temperature using circular ROIs of 36-pixel diameter on individual cells in a field of view containing a second fluorescent cell with a ROI for the photobleaching control and space outside the cells with a ROI for the background control. The FRAP measurement included 30 iterations of prebleach imaging; 10 iterations of bleaching with 100% laser power at 458, 477, and 488 nm; and a recovery phase with image acquisition at maximum speed (~200–250ms).

For data processing, the fluorescence intensity trace of the FRAP ROI was corrected for photobleaching by dividing with

the fluorescence intensity trace of the photobleaching control ROI. Then it was normalized to the average prebleach value with the following expression,

$$\text{Intensity}_{\text{normalized}} = \frac{(I_F - I_F^{\text{photobleach}})}{(I_{\text{av.prebleach}} - I_F^{\text{photobleach}})} \quad \text{(Eq. 1)}$$

where I_F is the fluorescence intensity trace corrected for photobleaching, $I_F^{\text{photobleach}}$ is the fluorescence intensity value of the first point after photobleaching, and $I_{\text{av.prebleach}}$ corresponds to the averaged prebleach values. Then the traces of GPI-GFP fluorescence from different days in several cells treated or not with EqtII were compared and averaged (30, 31).

FRET Measurements—For FRET experiments, cells in buffer A were treated with 2.5 μg/ml EqtII-Alexa488 (donor-only sample), 2.5 μg/ml EqtII-Alexa555 (acceptor-only sample) or the combination of both versions of EqtII (FRET sample). Analysis of sensitized emission was carried out with Fiji software according to Jalink and co-workers (32). After 1 h of incubation at room temperature, three confocal images were acquired for each of the different samples under the same imaging conditions: 1) D images: samples were excited with 488-nm laser light, and fluorescence was collected using a BP filter 505–530 nm; 2) S images: samples were excited with 488-nm laser light, and fluorescence was collected with a BP filter 555–615 nm; and 3) A images: samples were excited with 543-nm laser light, and fluorescence was collected with a BP filter 555–615 nm. Correction factors were calculated using ROIs selected for cells in the donor-only and acceptor-only samples: for cross-excitation in the donor channel α, ROI intensity in image D was divided by that of image A for acceptor only; for cross-excitation in the acceptor channel γ, ROIs in the acceptor-only sample were selected and intensity of image S was divided by image A; for the donor-only sample, β was calculated by dividing the intensity of a ROI in the S image by that of the D image. Sensitized emission in the FRET samples was calculated by correcting its S image with the previous correction factors and the D and A images: S.E. = (S-βD-(γ-$\alpha\beta$)A)/(1-$\beta\alpha/\gamma$). The apparent efficiency was calculated by normalizing the sensitized emission image with the A image of the FRET sample.

For experiments of FRET acceptor photobleaching, we performed time lapse confocal imaging with a multi-track configuration for acquisition under D, S, and A conditions (as above). The time series included 10 prebleach iterations, 100 bleach iterations (100% intensity of 543-nm laser) within a ROI defined on the cell surface and consecutive post-bleaching acquisition. FRET efficiency, %FRET, was calculated as:

$$\%\text{FRET} = \frac{I^D_{\text{postbleach}} - I^D_{\text{prebleach}}}{I^D_{\text{postbleach}}} \cdot 100 \quad \text{(Eq. 1)}$$

where I^D is the intensity of the ROI in the D images, and the subindexes prebleach and postbleach refer to the average intensity of the ROI before and after bleaching, respectively (33).

Fluorescence Cross-correlation Spectroscopy—Two-focus two-color scanning fluorescence cross-correlation spectroscopy was performed as described in Refs. 34 and 35. The measurements were carried out at room temperature (22 °C) on a LSM Meta 510 microscope (Zeiss) using a 40× NA 1.2 UV-visible IR C Apochromat water-immersion objective, the 488-nm line of an argon ion laser (25 μW), a 633-nm HeNe laser (15 μW), and a home-built detection unit at the fiber output channel. A dichroic mirror and band pass filters (D555, HQ520/40, and HQ700/75; AHF Analysetechnik, Tuebingen, Germany) were used behind a collimating achromat to split the emission for the dual color detection and to reject residual laser and background light. Achromats (LINOS Photonics, Goettingen, Germany) were then used to image the internal pinhole onto the apertures of the fibers connected to the avalanche photo diodes (PerkinElmer Life Sciences). The photon arrival times were recorded in the photon mode of the hardware correlator Flex 02–01D (Correlator.com, Bridgewater, NJ).

During measurements, the detection volume was repeatedly scanned perpendicularly through the equator of a plasma membrane bleb. The frame mode with 32 × 2 pixels in the LSM acquisition software was used to scan the two parallel lines. Their distance d was measured by repeatedly scanning over a film of dried fluorophores and measuring the distance between the bleached traces in a high resolution LSM Image. Data analysis was performed with home-made software written in MATLAB (MathWorks, Natick, MA). The photon stream was binned in bins of 2 μs and arranged as a matrix with every row corresponding to one line scan. Movements of the membrane were corrected for by calculating the position of the maximum of a running average over several hundred line scans and shifting it to the same column. An average over all of the rows was fitted with a Gaussian, and only the elements of each row between -2.5σ and 2.5σ were added to construct the intensity trace. The auto- and cross-correlation curves of the resulting intensity traces were computed with a multiple tau correlation algorithm and fitted with a nonlinear least squares fitting algorithm. In all FCS data processing, irregular curves resulting from major instabilities and identified by distortions of the curves and a systematic change in the intensity trace were excluded from further analysis. The resulting auto- and cross-correlation functions were fitted to analytical models as described in the supplemental materials.

RESULTS

Equinatoxin II Binds Quickly to the Plasma Membrane and Induces Blebbing and Cell Death—We investigated the effect of equinatoxin II on the plasma membrane of the target cells during its toxic action. To this end, we added increasing amounts of EqtII labeled with Alexa488 (EqtII-Al488) to HEK293T cells and followed the toxin effects by live cell imaging at 37 °C. As shown in the time lapse in Fig. 1*A* (and supplemental Movie S1), EqtII-Al488 can be detected on the target cells a few seconds after addition, indicating rapid binding to their plasma membrane. A few minutes later, most cells develop a single bleb that grows over time until the cells round up and finally collapse. Comparable results were obtained with other cell types such as HeLa Kyoto and COS7 (not shown).

Similar blebbing events have been reported in other animal cells under the attack of other pore-forming toxins, like in the case of streptolysin O and parasporin-2 (36, 37). Bleb appearance is probably a result of the detachment of a region of the plasma membrane from the actin meshwork of the cell cortex

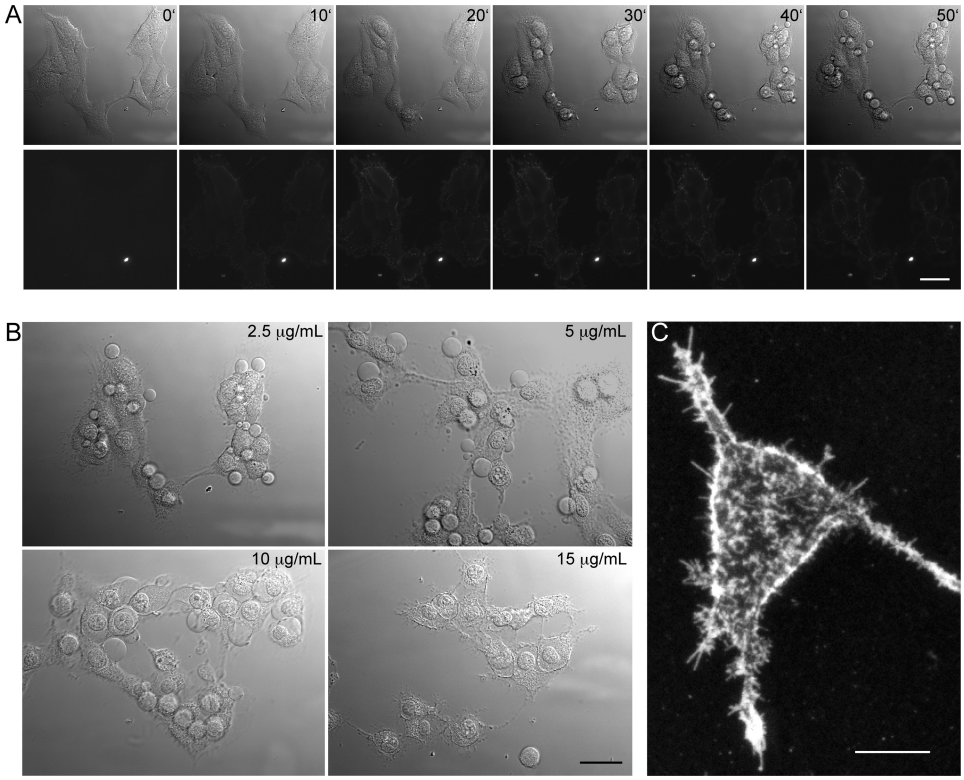

FIGURE 1. **EqtII binds rapidly to cells and induces plasma membrane blebbing.** *A*, time series of EqtIIAl488 action on HEK273 cells followed simultaneously by differential interference contrast and epifluorescence. The differential interference contrast images in the *top row* show the appearance of plasma membrane blebs that grow over time. In the *lower row*, binding of EqtII-Al488 can be detected by epifluorescence a shortly after toxin addition. *Scale bar*, 20 μm. *B*, the size of EqtII-induced blebs is concentration-dependent. The images show the state of HEK273 cells after a 1-h addition of the indicated EqtII amounts. *Scale bar*, 20 μm. *C*, confocal three-dimensional projection of a HEK273 cell 5 min after the addition of EqtII-Al488 shows heterogeneous distribution of the protein on the cell surface. *Scale bar*, 10 μm. Toxin concentration in *A* and *C* was 5 μg/ml.

caused by mechanical stress induced by the osmotic imbalance following the poration of the plasma membrane. Although the role of blebbing under pathological conditions is still controversial, it has been recently proposed that it has a defensive function against cell lysis (36, 37).

Membrane repair systems are additional mechanisms to combat the deadly consequences of membrane poration by PFPs. Depending on the extent and duration of the injury, cells can remove the damaged areas from the membrane by endocytosis and recover the integrity of their plasma membrane (2). However, these mechanisms do not seem to be effective in the case of EqtII attack at the concentrations investigated, because 1–2 h after toxin addition, the cells finally round up and collapse. A possible reason for this failure to repair EqtII-induced membrane injuries could be related to the small size of the pores induced. Similarly to EqtII, α-toxin or aerolysin form pores with ~2-nm diameter, and cells treated with these toxins had more difficulties or were unable to recover (38). However, the nature of the cell survival mechanisms in response to the attack of PFPs is still poorly understood. The alterations in membrane organization and cellular processes described below provide a molecular explanation that correlates with this effect.

As observed in Fig. 1*B*, the only apparent differences in the death of cells exposed to higher amounts of toxin consist in the faster appearance and growth of plasma membrane blebs and consequent cellular collapse. At the higher concentrations used, the cells rounded up and collapsed quickly without the formation of a bleb, indicating that this process depends on the concentration of toxin and, thus, the extent of membrane injury. These observations further support the protective role of membrane blebs upon EqtII attack.

Interestingly, EqtII-Al488 distribution on the cell membrane 5 min after addition (Fig. 1*C*) is far from homogeneous and seems to organize into defined toxin domains. This is in good agreement with observations made in *in vitro* experiments, in which the pore forming activity of the toxin is enhanced in membranes that exhibit lipid phase separation (19, 20). These considerations prompted us to investigate the changes in membrane organization in the presence of the toxin.

Equinatoxin II Clustering Reorganizes the Plasma Membrane and Leads to Formation of Microscopic Domains Where the Toxin Colocalizes with Raft Proteins—We transiently transfected COS7 cells with GPI-GFP, a version of GFP with a GPI anchor that targets the protein to the outer leaflet of the plasma membrane. We then investigated the distribution of the fluorescence protein during the toxic action of EqtII by live cell three-dimensional confocal imaging. As shown in Fig. 2*A* (time, 0 min), GPI-GFP is homogeneously distributed in the plasma membrane of cells, at least at the microscopic level. It also accumulates at the Golgi and the endoplasmic reticulum membranes. However, upon EqtII addition, GPI-GFP undergoes a rapid redistribution within the cellular membranes and, in just a few minutes, organizes into immobile, microscopic domains (Fig. 2*A* and supplemental Movie S2).

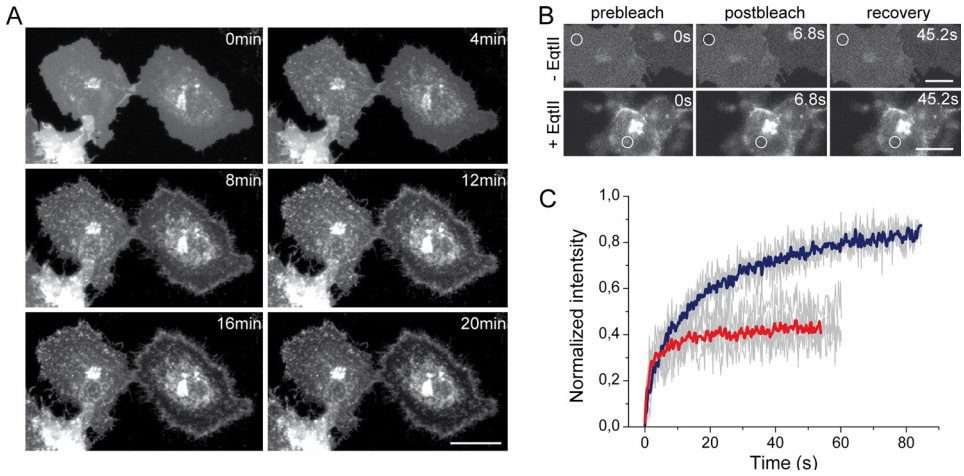

FIGURE 2. **EqtII induces plasma membrane reorganization.** *A*, time series of GPI-GFP redistribution in the membrane of COS-7 cells upon the addition of EqtII. The time points after toxin addition are indicated. The images are three-dimensional projections of confocal slices. *Scale bar*, 30 μm. *B*, FRAP experiments to characterize GPI-GFP dynamics in absence (*upper panel*) and presence (*lower panel*) of EqtII. Time points before and after bleaching and after the indicated recovery time are shown. The bleached areas correspond to the *white circles*. *Scale bar*, 20 μm. *C*, FRAP recovery curves of GPI-GFP fluorescence intensity in absence (*blue line*) and presence (*red line*) of EqtII. Curves are averages of five measurements, and original curves are shown in *gray*. Toxin concentration was 5 μg/ml.

To investigate whether GPI-GFP redistribution in the presence of EqtII is accompanied by changes in membrane fluidity and/or submicroscopic organization, we performed FRAP experiments. In these measurements, the mobility of GPI-GFP within the plasma membrane was compared in the absence and presence of EqtII. A small, circular region of the cell was subjected to a short pulse of high intensity laser illumination so that most of the GPI-GFP fluorophores within the region were photobleached (Fig. 2*B*). The recovery of fluorescence intensity caused by GPI-GFP diffusion into the fluorophore-depleted area is then quantified as a function of time. Fig. 2*C* shows the kinetics of GPI-GFP fluorescence recovery in cells before and after treatment with EqtII. Compared with untreated cells, GPI-GFP exhibits faster recovery kinetics and a larger immobile fraction in cells incubated with EqtII. These effects have been associated with the transition into a less homogeneous, compartmentalized membrane (39). These results indicate that after membrane binding, EqtII induces the reorganization of the plasma membrane into a more compartmentalized environment, where GPI-GFP and also EqtII-Al488 cluster into immobile domains of microscopic size.

EqtII binds specifically to SM, a lipid that has been involved in the formation of rafts (16, 40). Moreover, other toxins of the same family have been found associated with the fraction of detergent-resistant membranes in isolation experiments (17). Based on this, we decided to investigate whether the toxic domains observed in treated cells present raft characteristics. For this purpose, we characterized the colocalization of EqtII with conventional raft and nonraft proteins during the toxic action of EqtII by three-dimensional confocal live cell imaging.

As with GPI-GFP, when EqtII-Atto655 was added to cells transfected with common raft markers like Myr-Pal-YFP or LAT-GFP (24, 25, 41, 42), a profound reorganization of the fluorescent proteins was observed in the course of a few minutes (Fig. 3 and supplemental Movies S3–S5). In addition, EqtII-Atto655 accumulated on the microscopic domains enriched in the labeled raft proteins, indicating a colocalization

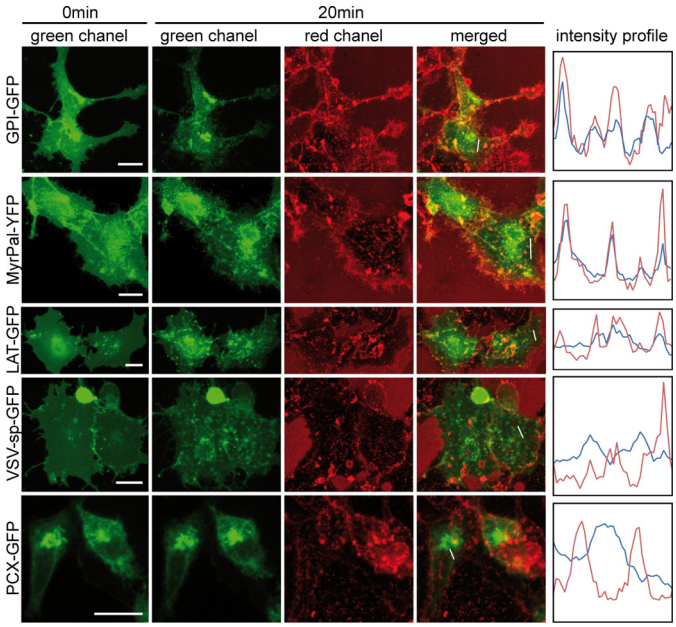

FIGURE 3. **EqtII colocalizes with raft markers on the plasma membrane.** COS-7 cells transfected with the indicated plasma membrane proteins fused to fluorescent proteins were treated with EqtII-Atto655, and the distribution of the fluorescent markers was followed by three-dimensional time lapse microscopy (supplemental Movies S3–S7). The changes in protein distribution before (0 min) and 20 min after toxin addition are shown as Z projections. The colocalization between EqtII (*red lines*) and raft-associated GPI-GFP, Myr-Pal-YFP and LAT-GFP (*blue lines*) is shown in the column with intensity profiles corresponding to the *white lines* in the merged channels. In contrast, colocalization with non-raft-associated VSV-sp-GFP and PCX-GFP is not evident. *Scale bar*, 20 μm.

of both molecules. In contrast, the effect of EqtII-Atto655 on cells transfected with nonraft membrane proteins was different (25, 26). In the case of VSV-sp-GFP, the distribution of the fluorescent protein was also altered with similar kinetics in the presence of EqtII. However, we failed to observe comparable levels of colocalization of the VSV-sp-GFP enriched domains and the EqtII domains (Fig. 3 and supplemental Movie S6). In other cases, as with PCX-GFP, protein distribution did not even

change apparently in the presence of the toxin, and colocalization was not observed either (Fig. 3 and supplemental Movie S7).

To analyze the significance of the colocalization results shown in Fig. 3, we carried out a quantitative analysis and calculated the two-dimensional colocalization histograms and the Pearson's coefficient for the fluorescence signal detected in the red channel (EqtII-Al633) and the green channel (GFP- or YFP-labeled membrane markers) (see supplemental Fig. S1). We obtained Pearson's coefficients of 0.677 and 0.553 for colocalization of EqtII-Al633 with GPI-GFP and MyrPal-YFP, respectively, and 0.214 and 0.213 for colocalization of EqtII-Al633 with VSV-sp-GFP and PCX-GFP, respectively. These results quantitatively show a higher degree of localization of EqtII with the raft-associated proteins GPI-GFP and MyrPal-GFP than for VSV-GFP and PCX-GFP, normally not associated with rafts. For LAT-GFP with EqtII-Al633, we obtained a Pearson's coefficient of 0.334, indicative of an intermediate situation, in agreement with the overlap of their intensity profiles.

Altogether, these results indicate that EqtII reorganizes the plasma membrane during its toxic action and induces the formation of immobile domains of microscopic size. Moreover, these domains differ in nature; although proteins traditionally associated with lipid rafts colocalize with EqtII domains, non-raft proteins are enriched in different domains devoid of EqtII or do not significantly alter their organization in the presence of the toxin.

Equinatoxin II Membrane Permeabilization Is Accompanied by Ca^{2+} Entry, PI(4,5)P_2 Degradation, Endocytosis Inhibition, and Alterations of the Actin Cytoskeleton—Lipid rafts are believed to be small (10–200 nm), heterogeneous, and highly dynamic domains enriched in sterols and sphingolipids. They compartmentalize cellular processes and can sometimes be stabilized to form larger platforms through protein-protein and protein-lipid interactions (43). The nature of the microscopic, immobile domains induced by EqtII that we observe appears to be different.

If one takes into account the forces driving raft clustering, nanodomains should grow continuously to reach microscopic size (44). However, this would likely not be compatible with cell metabolism, and a number of cellular processes have been proposed to play a role in counteracting this effect and keeping the size of rafts at the nanoscale. For instance, the endocytic pathway has been proposed to be involved in the removal of clustered rafts once they reach a critical size (13). Interestingly, similar mechanisms have been associated with the removal of membrane injuries during the attack of membrane-active toxins (2). Another possibility could be a potential mixing effect of the cytoskeleton on the lateral organization of the plasma membrane that would hinder raft coalescence (13). In both cases, the contacts between membrane and cytoskeleton would have an important role. Taking this into account, we investigated how cellular processes associated with avoiding raft growth to microscopic size are perturbed during the toxic action of EqtII.

The increase in calcium concentration in the cytosol upon membrane injury is held responsible for many of the alterations in cellular pathways and their deadly consequences (2, 38). Indeed, rapid elevations of cytosolic Ca^{2+} levels following membrane injury alter the cytoskeleton and its contacts with the membrane (27, 45). To detect possible increases in cytosolic Ca^{2+} associated with EqtII-induced membrane permeabilization, we treated the cells with the nonfluorescent acetoxymethyl ester of Fluo4, which is cleaved inside cells to yield the free, fluorescent form of the calcium indicator (46). As shown in Fig. 4*A* (*upper panel*), a clear increase in calcium concentration was detected in the cytosol of cells a few minutes after adding EqtII. Increases in cytosolic Ca^{2+} have been associated with the degradation of PI(4,5)P_2, a lipid of the plasma membrane that has been involved in contacts with the cytoskeleton (27). We used the specific PI(4,5)P_2 marker PH(PLC)GFP to analyze the effect of EqtII on this lipid (47). The redistribution of the probe to the cytosol shown in Fig. 4*A* (*lower panel*) is indicative of PI(4,5)P_2 disappearance from the plasma membrane, concomitant with Ca^{2+} entry after EqtII treatment. As a control, no increase of Fluo4 fluorescence or redistribution of PH(PLC)GFP was detected upon addition of EqtII to cells incubated in a calcium-free buffer (see controls in Fig. 4*A*). Interestingly, we still observed reorganization of GPI-GFP upon EqtII treatments in the absence of Ca^{2+} (see supplemental Fig. S2).

To investigate possible alterations in the endocytic pathway as a consequence of EqtII action, we monitored the internalization of cholera toxin subunit B labeled with Al488 (CTB-Al488). CTB binds specifically to the ganglioside GM1, a lipid associated with lipid rafts and is then internalized (see control in Fig. 4*D*) by clathrin-dependent as well as by caveolae- and clathrin-independent endocytosis (48). Interestingly, CBT-Al488 colocalized with EqtII-Atto655 domains similarly to the other raft-associated proteins we tested in Fig. 3 (not shown).

As observed in Fig. 4*B*, CTB-Al488 was largely internalized after 2 h of incubation before adding EqtIIAtto655. However, the levels of endocytosed CTB significantly decreased when EqtII was added just after 5 min of incubation with CTB-Al488 and were negligible when both molecules were added simultaneously. The quantification of these observations is shown in Fig. 4*C*. These results indicate that endocytic trafficking is disrupted right after the addition of EqtII, suggesting a strong effect of the toxin activity on this process.

Endocytosis is heavily dependent on cytoskeleton dynamics, which in turn have also been associated with a mixing effect that would avoid microscopic raft clustering. To investigate alterations in cytoskeleton dynamics induced by EqtII action, we transfected cells with Lifeact-GFP, a specific marker for F-actin that has been shown not to interfere with its function (28). We followed actin dynamics upon EqtII addition by three-dimensional live cell confocal imaging. As observed in Fig. 4*E*, EqtII induced an abnormal reorganization of the actin cytoskeleton. It was characterized by stabilization of actin stress fibers, condensation around the nucleus, and formation of a dense meshwork within the same time range as the other cellular alterations induced by the toxin. Interestingly, a decrease in the dynamic behavior of the actin structures was observed.

As a control of the dependence of cellular alterations on the membrane permeabilizing activity of EqtII, we used a mutant form of the toxin that contains two additional Cys that form a disulfide bridge and inhibit the exposure of helix 1 upon membrane binding, which is necessary for pore formation (23, 50).

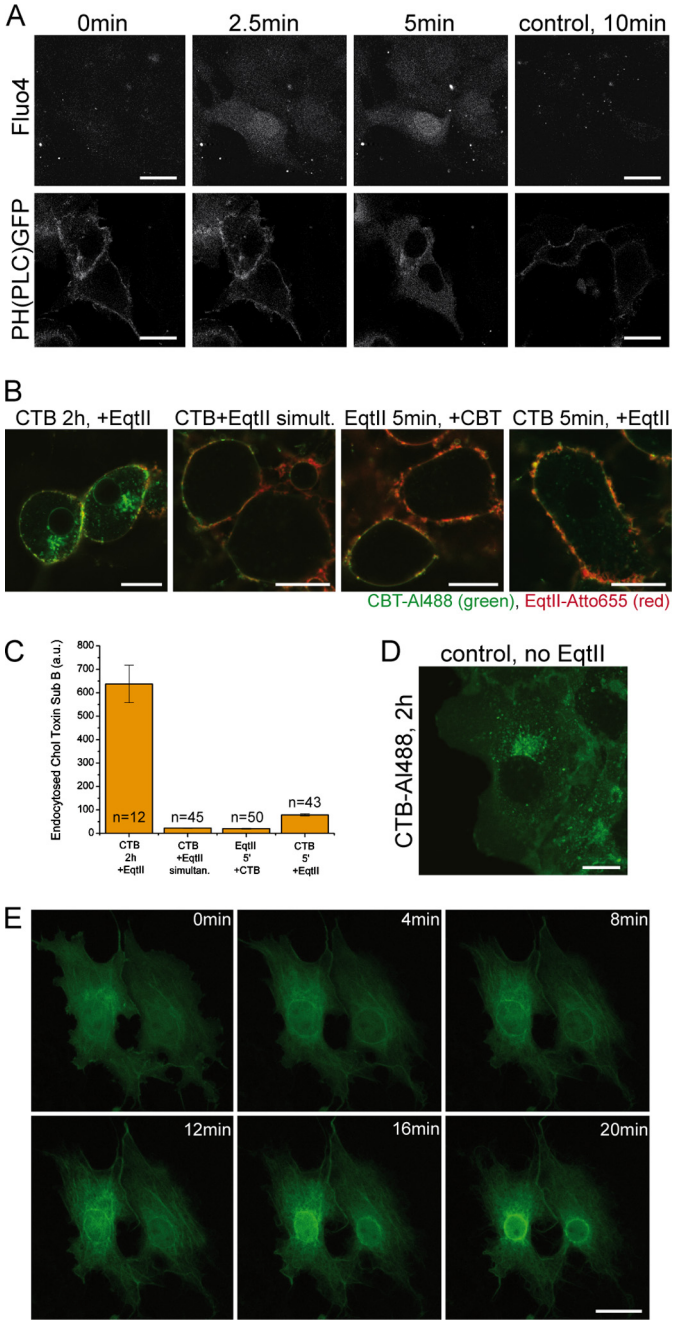

FIGURE 4. **EqtII action induces Ca^{2+} entry, PI(4,5)P_2 degradation, endocytosis inhibition and reorganization of the actin cytoskeleton.** *A*, addition of EqtII induces an increase in intracellular Ca^{2+} in a few minutes (*upper panel*). This correlates with degradation of PI(4,5)P_2 at the plasma membrane, as shown by the reorganization of PH(PLC)GFP fluorescence within the same time range. In contrast, Fluo4 signal does not show any increase, and PI(4,5)P_2 signal is maintained at the plasma membrane when a buffer without Ca^{2+} is used (controls, 10 min). *Scale bars*, 25 μm. *B*, CTB-Al488 endocytosis is inhibited after the addition of EqtII. The *first panel* shows CTB-Al488 that has been endocytosed when it is added 2 h before EqtII. In the *second* and *third panels*, CTB-Al488 is not endocytosed when EqtII is added simultaneously or 5 min before CTB-Al488. The *fourth panel* shows small amounts of endocytosis when CBT-Al488 is added 5 min before EqtII. In all cases, the cells were analyzed after 1 h of incubation with EqtII at room temperature. *Scale bar*, 15 μm. *C*, quantification of endocytosed CTB-Al488 in the samples shown in *B*. The number of cells analyzed in each sample is shown. *D*, control of CBT-Al488 endocytosis after 1 h in the absence of EqtII. *Scale bar*, 15 μm. *E*, reorganization of actin cytoskeleton upon EqtII addition. Actin filaments stained with Lifeact-GFP underwent reorganization within the same time scales as the redistribution of membrane markers (Figs. 2 and 3). COS-7 cells were used in all experiments. *Scale bar*, 25 μm.

To ensure that the disulfide bond was formed, we oxidized the protein with 1,10-phenantroline and $CuSO_4$ prior to use. This EqtII mutant did not induce cell death within a similar range of concentrations and times as compared with the wild type protein (not shown). In agreement with this, Ca^{2+} entry into the cytosol was not detected when cells were incubated with mutant EqtII-Atto655 up to 1 h (supplemental Fig. S4*A*).

Although this mutant bound heterogeneously to the plasma membrane of the target cells (supplemental Fig. S4*B*, *lower panel*), no significant GPI-GFP reorganization could be observed in the presence of EqtIIAtto655 mutant (supplemental Fig. S3). This indicates that membrane permeabilization is necessary for the growth of microscopic domains. Moreover, the inactive toxin did not inhibit endocytosis as readily as the wild type EqtII. Indeed, a significant portion of the mutant was internalized 1 h after addition to the cells (supplemental Fig. S4*B*). Finally, the actin cytoskeleton and its dynamics were not affected either (supplemental Fig. S4*C*).

Equinatoxin II Action Is Associated with Oligomerization—As for other toxins of the family, EqtII pore formation has been associated with the ability of the protein to form oligomers. However, so far EqtII oligomerization has not been shown in living cells. On the other hand, the specific binding of EqtII to sphingomyelin and consecutive oligomerization would provide the basis for the clustering of raft components, which is compatible with the formation of microscopic domains that we observe.

To investigate the oligomerization of EqtII in living cells, we performed experiments of FRET microscopy. In these experiments, we used mixtures of EqtII labeled with Alexa488 (donor) and with Alexa555 (acceptor). Direct protein/protein interactions bring the fluorophores in close proximity, so that excited EqtII-Al488 can transfer nonradiative energy to EqtII-Al555, whose subsequent fluorescent emission can be detected. The FRET efficiency depends on the overlap between the emission and absorption spectra of donor and acceptor, respectively; the relative orientation of their dipoles; and, importantly, the distance between the fluorophores, which in general should be less than 10 nm.

Fig. 5*A* shows the fluorescence of the donor after excitation at 488 nm, that of the acceptor when excited at 543 nm, the resulting sensitized FRET emission of the acceptor obtained when exciting at 488, and the normalized, apparent FRET efficiency. The cross-excitation and cross-emission effects have been corrected as explained under "Experimental Procedures." The calculated FRET image shows the spatial distribution of FRET fluorescence, which coincides with the domains enriched in EqtII and indicates the existence of protein/protein interactions between EqtII molecules in these regions. From these experiments it is not possible to extract the stoichiometry, but the strong FRET signal is compatible with toxin oligomers.

To support our results of sensitized FRET microscopy, we performed experiments of acceptor photobleaching, which provide direct evidence of FRET and, thus, protein/protein interactions. As shown in Fig. 5*B*, when we photobleached EqtII-Al555 in a small region of the cell with high intensity laser light of 543 nm, the fluorescence emitted by the donor EqtII-Al488 clearly increased. The graph in Fig. 5*C* shows the changes

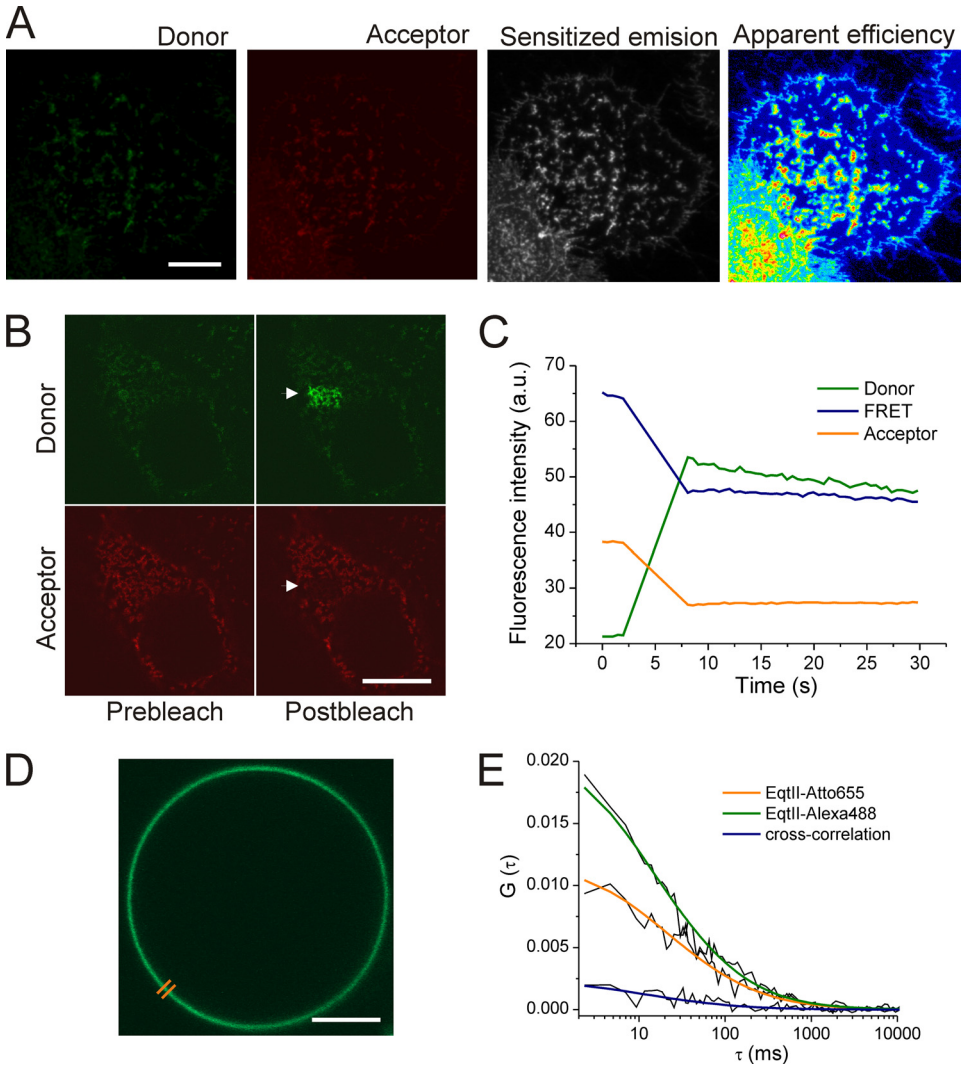

FIGURE 5. **EqtII oligomerizes on the plasma membrane of target cells.** *A–C*, EqtII oligomerization shown by FRET. EqtII-Al488 (donor) and EqtII-Al555 (acceptor) were added to COS-7 cells and incubated for 1 h at room temperature. In *A*, the fluorescence of the donor and acceptor channels is shown in the *first* and *second panels*, respectively. The *third panel* shows the calculated sensitized emission FRET for the same region, which is normalized to apparent FRET efficiency in the *fourth panel*. The color code goes from black for minimum *gray* values to *blue*, *green*, *yellow*, *orange*, *red*, and then *white* for maximum gray values. *Scale bar*, 15 μm. In *B*, EqtII oligomerization is shown by acceptor photobleaching FRET. The increase in the donor fluorescence in the region indicated with an arrow (*upper panel*) upon acceptor photobleaching within that region via high intensity illumination (*lower panel*) is a direct evidence of EqtII/EqtII interactions. *C*, time changes in the fluorescence detected in donor, acceptor, and FRET channels upon acceptor photobleaching. *D* and *E*, direct EqtII/EqtII interactions shown by two-color two-focus scanning FCS. COS-7 cells were treated with Eqt-Al488 and EqtII-Atto655 and incubated for 1 h at room temperature. FCS was measured on the membrane of cell blebs induced by the toxin. *D*, the two foci of scanning FCS are depicted as *parallel lines* on one of the blebs measured. *E*, auto- and cross-correlation fitted curves of EqtII-Al488 and EqtII-Atto655. The positive amplitude of the cross-correlation curve (*blue line*) indicates direct EqtII/EqtII interactions. Raw data are shown in *black lines*. *Scale bars*, 15 μm.

in fluorescence intensity of the donor and the acceptor before and after acceptor photobleaching. From these values, we estimated a FRET efficiency of ~60% (see "Experimental Procedures").

As additional evidence of EqtII oligomerization in cells, we performed two-color two-focus scanning FCS on the membrane of the membrane blebs induced by EqtII. Two-color FCS is a method with single molecule sensitivity that detects dynamic colocalization of the fluorophores by analyzing the coincidence of fluorescence fluctuations (34, 51, 52). It is independent of dipole orientation, fluorescence intensity, and distance between the fluorophores, as long as they are contained within the confocal volume of the microscope. However, it needs spatially homogeneous membranes, the reason why we measured on the plasma membrane blebs. In our experiments, we used EqtII forms labeled with spectrally different fluorophores (EqtII-Al488 and EqtII-Atto655). Fig. 5*D* shows an example of a cellular bleb and the two lines we scanned with the FCS. As shown on Fig. 5*E*, the cross-correlation analysis of the fluorescence fluctuations detected in the green and red channels yields a cross-correlation curve with positive amplitude, which is indicative of interactions between EqtII molecules within the membrane of the toxin-induced blebs, in agreement with the results obtained in the FRET experiments.

DISCUSSION

In this work we have investigated the alterations in the plasma membrane of target cells induced by the toxic action of EqtII. We found that as a consequence of the toxin attack, the cell body shrinks, and a bleb grows out of the plasma membrane

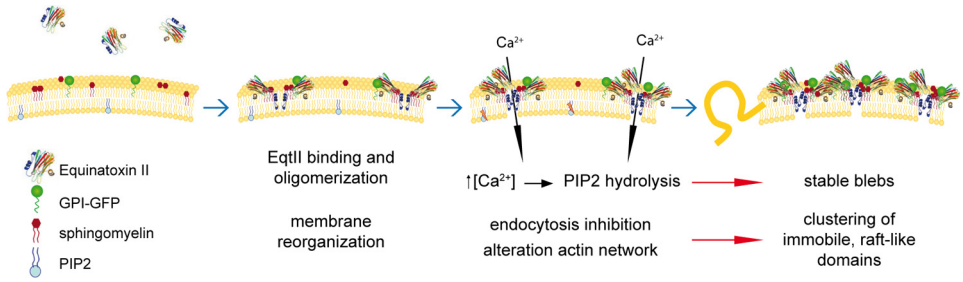

FIGURE 6. **Model of EqtII-induced membrane reorganization during its toxic action.** EqtII binds specifically to the SM exposed in the outer leaflet of the plasma membrane of cells and oligomerizes to form a pore. This allows calcium entry into the cytosol, which among other effects induces PI(4,5)P_2 degradation, and endocytosis and cytoskeleton dynamics are inhibited. As a result, the alterations in membrane traffic affect the membrane repair machinery, and EqtII oligomers are not internalized, thus growing to immobile microscopic domains that accumulate other raftophilic proteins. In addition, membrane links to the cytoskeleton are disrupted and, together with osmotic imbalance, lead to the growth of stable blebs. Finally, EqtII-induced transformation into a dysfunctional plasma membrane, whose lateral organization and permeability are compromised, leads to cell death.

prior to cell round-up and collapse. These changes have been attributed to the disruption of cellular homeostasis because of the osmotic imbalance created by the toxin-induced membrane injuries. Bleb growth correlated with an increase in cytosolic calcium concentration and PI(4,5)P_2 degradation at the plasma membrane, which have been associated with irreversible bleb formation probably because of a weakening of membrane/cytoskeleton contacts (27).

One of the most striking observations we made is the reorganization of proteins of the plasma membrane a few minutes after EqtII addition. We found that EqtII induces the formation of microscopic domains during the initial attack steps and clearly before cells die, which under our conditions usually happened between 1 and 2 h after toxin treatment. This indicates that the observed membrane reorganization is a consequence of EqtII action and not an artifact produced by dead cells. Our results show that toxin binding and pore formation have a profound effect on the lateral organization of the plasma membrane, and thus, it is tempting to speculate that such alterations form part of the deadly strategy of the toxin.

One interesting aspect of EqtII-induced membrane reorganization is that the toxin induces the formation of domains enriched in proteins traditionally associated with lipid rafts and colocalizes with them. It has been shown that EqtII binds specifically to sphingomyelin, a raft lipid, and that it oligomerizes to form pores (4, 16). Our FRET experiments on living cells also show EqtII/EqtII interactions within the toxin-induced domains. These observations are compatible with clustering of sphingomyelin concomitant with EqtII oligomerization and pore formation, which would bring together other cellular components of rafts. Hence, we hypothesize that the domains induced by and enriched in EqtII are stabilized rafts that reach microscopic sizes. Interestingly, the ability of the plasma membrane of mammalian cells to segregate into microscopic domains with raft properties has been reported in a number of studies (42, 53, 54).

However, rafts do not reach microscopic dimensions in cells under normal conditions (13). To achieve this, it is believed that a number of mechanisms are in place that counteract the energy gain associated with raft coalescence and avoid their clustering into big structures that would compromise their functional role in signaling, trafficking, and partitioning. In this context, the action of EqtII must somehow alter or imbalance these cellular processes so that the formation of microscopic raft domains is possible.

Our results show that the formation of microscopic domains is independent of the increase of Ca^{2+} levels in the cytosol and of consequent PI(4,5)P_2 degradation at the plasma membrane that follow after toxin-induced membrane injury. However, an immediate consequence of EqtII pore formation is the inhibition of endocytosis, which correlates with changes in the dynamics of the actin cytoskeleton. The molecular details linking pore formation and inhibition of endocytosis and actin dynamics remain unclear, but these alterations could be related with each other and associated with the ionic imbalances and ATP depletion caused by permeabilization of the plasma membrane (2). It is important to note that domain formation, as well as endocytosis inhibition and actin network modifications, are dependent on EqtII-induced permeabilization of the plasma membrane. Indeed, the inactive mutant of EqtII, which still binds to sphingomyelin in membranes and has no modifications in its oligomerization domains, is unable to induce GPI-GFP reorganization and to inhibit endocytosis and cytoskeleton dynamics. In this sense, and in contrast to active EqtII, the pore-defective EqtII mutant was successfully internalized after binding to the plasma membrane.

Regardless of the mechanisms involved, our results show that both endocytosis inhibition and cytoskeleton alterations correlate with the growth of microscopic domains with raft properties and support a possible role for these processes in maintaining the size of lipid rafts in the nanometer range compatible with their function under normal conditions.

From our results and the data in the literature, we can propose a model for the action of EqtII (Fig. 6). Upon specific binding to sphingomyelin in the plasma membrane of the target cell, EqtII oligomerizes, forms a pore on the membrane, and then allows the passage of ions and small molecules. As a consequence, cytosolic Ca^{2+} levels increase, PI(4,5)P_2 at the plasma membrane is degraded, and endocytosis and cytoskeleton dynamics are inhibited. Simultaneously, toxin oligomerization brings together sphingomyelin and other raft components that cluster into immobile domains of microscopic size. At later steps, the disruption of membrane/cytoskeleton interactions and osmotic imbalance drive the growth of a membrane bleb. Finally, when the cell cannot cope with the stress induced by the membrane injuries, it swells and collapses.

Many PFPs recognize raft components in the target cell. Based on this, it has been proposed that the latter serve both as receptors and as concentration platforms (2). Interestingly, Gekara and Weiss (49) reported raft clustering under the effect of listeriolysin O. Taking this into account together with our results, it is tempting to speculate that raft clustering could be a general mechanism of PFPs that bind to raft components. Of importance, this possibility would imply the evolution of PFPs to exploit the lateral organization of eukaryotic cells into lipid rafts for their toxic action.

In summary, our results show that EqtII induces a drastic reorganization of the plasma membrane associated with toxin oligomerization, endocytosis inhibition, and alterations of the actin network. Interestingly, EqtII colocalizes with immobile, microscopic domains that resemble stabilized rafts. To our best knowledge, this is the first time that such effects on membrane organization are reported. Altogether, toxin-induced alterations of the plasma membrane produce a dysfunctional membrane whose lateral organization, dynamics, and permeability are compromised, all of this being incompatible with cell homeostasis and leading to cell death.

Acknowledgments—We thank K. Krell, H. Hartmann, Peter Bankhead, and J. C. Olaya for technical assistance.

REFERENCES

1. Anderluh, G., and Lakey, J. H. (2008) *Trends Biochem. Sci.* **33,** 482–490
2. Bischofberger, M., Gonzalez, M. R., and van der Goot, F. G. (2009) *Curr. Opin. Cell Biol.* **21,** 589–595
3. Kleanthous, C. (2010) *Nat. Rev. Microbiol* **8,** 843–848
4. Belmonte, G., Pederzolli, C., Macek, P., and Menestrina, G. (1993) *J. Membr. Biol.* **131,** 11–22
5. Mancheño, J. M., Martín-Benito, J., Gavilanes, J. G., and Vázquez, L. (2006) *Biophys. Chem.* **119,** 219–223
6. Martín-Benito, J., Gavilanes, F., de Los Ríos, V., Mancheño, J. M., Fernández, J. J., and Gavilanes, J. G. (2000) *Biophys. J.* **78,** 3186–3194
7. Mueller, M., Grauschopf, U., Maier, T., Glockshuber, R., and Ban, N. (2009) *Nature* **459,** 726–730
8. Mechaly, A. E., Bellomio, A., Gil-Cartón, D., Morante, K., Valle, M., González-Mañas, J. M., and Guérin, D. M. (2011) *Structure* **19,** 181–191
9. Anderluh, G., Dalla Serra, M., Viero, G., Guella, G., Macek, P., and Menestrina, G. (2003) *J. Biol. Chem.* **278,** 45216–45223
10. Anderluh, G., Barlic, A., Potrich, C., Macek, P., and Menestrina, G. (2000) *J. Membr. Biol.* **173,** 47–55
11. Tejuca, M., Dalla Serra, M., Potrich, C., Alvarez, C., and Menestrina, G. (2001) *J. Membr. Biol.* **183,** 125–135
12. Gonzalez, M. R., Bischofberger, M., Pernot, L., van der Goot, F. G., and Frêche, B. (2008) *Cell Mol. Life Sci.* **65,** 493–507
13. Lingwood, D., and Simons, K. (2010) *Science* **327,** 46–50
14. Tweten, R. K., Parker, M. W., and Johnson, A. E. (2001) *Curr. Top. Microbiol Immunol.* **257,** 15–33
15. Nelson, K. L., Raja, S. M., and Buckley, J. T. (1997) *J. Biol. Chem.* **272,** 12170–12174
16. Bakrac, B., and Anderluh, G. (2010) *Adv. Exp. Med. Biol.* **677,** 106–115
17. Alegre-Cebollada, J., Rodríguez-Crespo, I., Gavilanes, J. G., and del Pozo, A. M. (2006) *FEBS J.* **273,** 863–871
18. Abe, Y., Shimada, H., and Kitada, S. (2008) *J. Biochem.* **143,** 269–275
19. Barlic, A., Gutiérrez-Aguirre, I., Caaveiro, J. M., Cruz, A., Ruiz-Argüello, M. B., Pérez-Gil, J., and González-Mañas, J. M. (2004) *J. Biol. Chem.* **279,** 34209–34216
20. Schön, P., García-Sáez, A. J., Malovrh, P., Bacia, K., Anderluh, G., and Schwille, P. (2008) *Biophys. J.* **95,** 691–698
21. Bakrac, B., Kladnik, A., Macek, P., McHaffie, G., Werner, A., Lakey, J. H., and Anderluh, G. (2010) *J. Biol. Chem.* **285,** 22186–22195
22. Malovrh, P., Viero, G., Serra, M. D., Podlesek, Z., Lakey, J. H., Macek, P., Menestrina, G., and Anderluh, G. (2003) *J. Biol. Chem.* **278,** 22678–22685
23. Kristan, K., Podlesek, Z., Hojnik, V., Gutiérrez-Aguirre, I., Guncar, G., Turk, D., González-Mañas, J. M., Lakey, J. H., Macek, P., and Anderluh, G. (2004) *J. Biol. Chem.* **279,** 46509–46517
24. Meder, D., Shevchenko, A., Simons, K., and Füllekrug, J. (2005) *J. Cell Biol.* **168,** 303–313
25. Meder, D., Moreno, M. J., Verkade, P., Vaz, W. L., and Simons, K. (2006) *Proc. Natl. Acad. Sci. U.S.A.* **103,** 329–334
26. Keller, P., Toomre, D., Díaz, E., White, J., and Simons, K. (2001) *Nat. Cell Biol.* **3,** 140–149
27. Keller, H., Lorizate, M., and Schwille, P. (2009) *Chemphyschem* **10,** 2805–2812
28. Riedl, J., Crevenna, A. H., Kessenbrock, K., Yu, J. H., Neukirchen, D., Bista, M., Bradke, F., Jenne, D., Holak, T. A., Werb, Z., Sixt, M., and Wedlich-Soldner, R. (2008) *Nat. Methods* **5,** 605–607
29. Ohrt, T., Mütze, J., Staroske, W., Weinmann, L., Höck, J., Crell, K., Meister, G., and Schwille, P. (2008) *Nucleic Acids Res.* **36,** 6439–6449
30. Goehring, N. W., Chowdhury, D., Hyman, A. A., and Grill, S. W. (2010) *Biophys. J.* **99,** 2443–2452
31. Charrier, C., Machado, P., Tweedie-Cullen, R. Y., Rutishauser, D., Mansuy, I. M., and Triller, A. (2010) *Nat. Neurosci.* **13,** 1388–1395
32. van Rheenen, J., Langeslag, M., and Jalink, K. (2004) *Biophys. J.* **86,** 2517–2529
33. Loose, M., Fischer-Friedrich, E., Herold, C., Kruse, K., and Schwille, P. (2011) *Nat. Struct. Mol. Biol.* **18,** 577–583
34. García-Sáez, A. J., Ries, J., Orzáez, M., Pérez-Payà, E., and Schwille, P. (2009) *Nat. Struct. Mol. Biol.* **16,** 1178–1185
35. Ries, J., Petrasek, Z., Garcia-Saez, A. J., and Schwille, P. (2010) *New J. Phys.* **12,** 32
36. Babiychuk, E. B., Monastyrskaya, K., Potez, S., and Draeger, A. (2011) *Cell Death Differ.* **18,** 80–89
37. Kitada, S., Abe, Y., Maeda, T., and Shimada, H. (2009) *Toxicology* **264,** 80–88
38. Gonzalez, M. R., Bischofberger, M., Frêche, B., Ho, S., Parton, R. G., and van der Goot, F. G. (2011) *Cell. Microbiol.***13,** 1026–1043
39. Saxena, R., and Chattopadhyay, A. (2011) *J. Neurochem.* **116,** 726–733
40. Bakrac, B., Gutiérrez-Aguirre, I., Podlesek, Z., Sonnen, A. F., Gilbert, R. J., Macek, P., Lakey, J. H., and Anderluh, G. (2008) *J. Biol. Chem.* **283,** 18665–18677
41. Harder, T., and Kuhn, M. (2000) *J. Cell Biol.* **151,** 199–208
42. Levental, I., Lingwood, D., Grzybek, M., Coskun, U., and Simons, K. (2010) *Proc. Natl. Acad. Sci. U.S.A.* **107,** 22050–22054
43. Pike, L. J. (2006) *J. Lipid Res.* **47,** 1597–1598
44. García-Sáez, A. J., Chiantia, S., and Schwille, P. (2007) *J. Biol. Chem.* **282,** 33537–33544
45. Janmey, P. A., and Lindberg, U. (2004) *Nat. Rev. Mol. Cell Biol.* **5,** 658–666
46. Zorec, R., Tester, M., Macek, P., and Mason, W. T. (1990) *J. Membr Biol.* **118,** 243–249
47. Stauffer, T. P., Ahn, S., and Meyer, T. (1998) *Curr. Biol.* **8,** 343–346
48. Torgersen, M. L., Skretting, G., van Deurs, B., and Sandvig, K. (2001) *J. Cell Sci.* **114,** 3737–3747
49. Gekara, N. O., and Weiss, S. (2004) *Biochem. Soc. Trans.* **32,** 712–714
50. Hong, Q., Gutierrez-Aguirre, I., Barlic, A., Malovrh, P., Kristan, K., Podlesek, Z., Macek, P., Turk, D., Gonzalez-Manas, J. M., Lakey, J. H., and Anderluh, G. (2002) *J. Biol. Chem.* **277,** 41916–41924
51. García-Sáez, A. J., and Schwille, P. (2008) *Methods* **46,** 116–122
52. García-Sáez, A. J., Carrer, D. C., and Schwille, P. (2010) *Methods Mol. Biol.* **606,** 493–508
53. Lingwood, D., Ries, J., Schwille, P., and Simons, K. (2008) *Proc. Natl. Acad. Sci. U.S.A.* **105,** 10005–10010
54. Baumgart, T., Hammond, A. T., Sengupta, P., Hess, S. T., Holowka, D. A., Baird, B. A., and Webb, W. W. (2007) *Proc. Natl. Acad. Sci. U.S.A.* **104,** 3165–3170